Mineralization of Methyl Orange azo dye by processes based on H_2O_2 electrogeneration at a 3D-like air-diffusion cathode

Ana A. Márquez [a], Ignasi Sires [b,1], Enric Brillas [b,1], José L. Nava[a,*]

[a] *Departamento de Ingeniería Geomática e Hidráulica, Universidad de Guanajuato, Av. Juárez 77, Zona Centro, 36000, Guanajuato, Guanajuato, Mexico*

[b] *Laboratori d'Electroquímica dels Materials i del Medi Ambient, Departament de Química Física, Facultat de Química, Universitat de Barcelona, Martí i Franquès 1-11, 08028 Barcelona, Spain*

E-mail addresses: aa.marquezvargas@ugto.mx (A. A. Márquez)
i.sires@ub.edu (I. Sirés)
brillas@ub.edu (E. Brillas)

* Corresponding's author e-mail address: jlnm@ugto.mx (J.L. Nava)

Abstract

This work addresses the mineralization of the widely used Methyl Orange (MO) azo dye by technologies based on H_2O_2 electrogeneration at a 3D-like air-diffusion cathode. These include two Fe^{2+}-catalyzed processes such as electro-Fenton (EF) and photoelectro-Fenton (PEF). Bulk electrolyses were performed in a recirculation flow plant, in which the Eco-Cell filter-press electrochemical reactor was connected in series with a UVA photoreactor. The former reactor was equipped with a Ti|Ir-Sn-Sb oxide plate anode alongside a 3D-like air-diffusion cathode made from graphite felt and hydrophobized carbon cloth, aimed at electrogenerating H_2O_2 on site. The influence of current density (*j*), volumetric flow rate (*Q*) and initial MO concentration was examined. The greatest oxidation power corresponded to PEF process. The best operation conditions to treat 30 mg L^{-1} of total organic carbon of MO in a 50 mM Na_2SO_4 solution by PEF were found at 0.50 mM Fe^{2+}, pH 3.0, j = 20 mA cm^{-2} and Q = 2.0 L min^{-1}, obtaining 100% and 94% of color and TOC removals at 240-300 min, respectively. This accounted for 35% of mineralization current efficiency and 0.12 kWh $(g\ TOC)^{-1}$ of energy consumption at the end of the electrolysis. The oxidation power of EF and PEF was compared with that of anodic oxidation (AO), and the sequence obtained was: PEF > EF > AO. The dye was gradually degraded, yielding non-toxic short carboxylic acids, like maleic, fumaric, formic, oxalic and oxamic, whose Fe(III) complexes were rapidly photolyzed.

Keywords: Azo dye; Gas-diffusion electrode; Hydrogen peroxide; Photoelectro-Fenton; Water treatment

1. Introduction

The incessant growth of industrial and urban activities has led to a progressive increase in the clean water demand. The resulting large volumes of wastewater are quite difficult to adequately manage through currently available technologies (McDonald et al., 2014; Cosgrove and Loucks, 2015). Many industries, from textile and leather to cosmetics or food employ synthetic dyes in their production chains, becoming a major source of contaminated aqueous effluents (Tkaczyk et al., 2020). The synthetic dyestuffs are categorized as persistent organic pollutant (POPs) because they tend to be designed with structural characteristics that confer them a high stability against hydrolysis, natural photolysis or biodegradation (Routoula and Patwardhan, 2020). For this reason, these dyes and some of their by-products are accumulated in water reservoirs, being ubiquitous in surface water in some countries (Bhatia et al., 2018), representing a huge risk to humans and the aquatic life (Khan and Malik, 2018).

The textile industry employs more than 30 million workers all over the world and the total production of synthetic dyes approaches 7×10^5 tons (Brillas and Martínez-Huitle, 2015; Desore and Narula, 2018). Azo dyes, characterized by the presence of at least one -N=N- functional group as chromophore linked to aromatic rings, constitute the main category with more than 70% of the produced dyestuffs (Rawat et al., 2016). Methyl Orange (MO) is an anionic monoazo dye (see characteristics in Table SM-1) widely used in the textile, printing and photographic industries (Guo et al., 2011). Although its impact on humans and animals has been scarcely reported, the genetic effects of azo dyes are well established (Chung, 2016). Therefore, a range of technologies has been investigated to remove MO from water. They include physical methods like adsorption (Arshadi et al., 2014) and chemical ones such as heterogeneous Fenton (Omri et al., 2020), heterogeneous

63 photocatalysis (Saravanan et al., 2018), anodic oxidation (AO) with various anodes (Zhou
64 et al., 2011; Chaiyont et al., 2013; Isarain-Chávez et al., 2017) and electro-Fenton (EF)
65 (Sirés et al., 2010; Jiang et al., 2016). In contrast, the photoelectro-Fenton (PEF) treatment
66 of MO solutions has not been investigated yet, which is a significant finding because this
67 is considered the most promising electrochemical advanced oxidation process (EAOP)
68 (Brillas, 2020).

69 Fenton-based EAOPs like EF and PEF processes have become increasingly popular for
70 the fast degradation of organic pollutants in water (Brillas and Martínez-Huitle, 2015;
71 Brillas and Sirés, 2015; Zhou et al., 2018; Brillas, 2020). The common feature of these
72 methods is the in-situ H_2O_2 electrogeneration from the cathodic reduction of O_2,
73 according to reaction (1) (Coria et al., 2015; Le et al., 2015; Scialdone et al., 2015; Zhou
74 et al., 2018; Salmerón et al., 2019), which is highly efficient at carbon-based materials
75 like carbon black (Lanzalaco et al., 2017; Lima et al., 2020), carbon nanotubes (Gendel
76 et al., 2014; Alcaide et al., 2020), graphene (Le et al., 2015; Yang et al., 2019), carbon
77 felt / graphite felt (El-Ghenymy et al., 2013; Lin et al., 2017; Pérez et al., 2018) or vitreous
78 carbon (González-Pérez and Bisang, 2014; Zhou et al., 2018). Some of these materials
79 have been implemented as cathodes that are simultaneously in contact with the conductive
80 solution and an air chamber fed with O_2 or air, in the so-called gas-diffusion electrodes
81 (GDE) conformation, which is the most suitable to produce H_2O_2 (El-Ghenymy et al.,
82 2013; Barazesh et al., 2015; Yu et al., 2015; Lanzalaco et al., 2017; Coria et al., 2018;
83 Salmerón et al., 2019; Lima et al., 2020).

84 $$O_2 + 2H^+ + 2e^- \rightarrow H_2O_2 \quad (1)$$

If the production of H_2O_2 takes place in the presence of dissolved Fe^{2+} (i.e., EF conditions), hydroxyl radicals ($^{\bullet}OH$) and Fe^{3+} are generated in the bulk via Fenton's reaction (2), whose optimum pH is ~3.0 (Brillas, 2020). Fe^{3+} can be reduced at the cathode to yield Fe^{2+} from reaction (3), which sustains the catalytic cycle (Brillas and Sirés, 2015). The organics present in such an oxidizing environment can be partially mineralized by $^{\bullet}OH$ in a non-selective manner, according to general reaction (4) (Martinez-Huitle et al., 2015).

$$Fe^{2+} + H_2O_2 \rightarrow Fe^{3+} + {}^{\bullet}OH + OH^- \quad (2)$$

$$Fe^{3+} + e^- \rightarrow Fe^{2+} \quad (3)$$

$$R + {}^{\bullet}OH \rightarrow CO_2 + H_2O \quad (4)$$

However, total mineralization is not feasible in EF, since very stable complexes between Fe(III) and some organic by-products are formed upon cleavage of the aromatic or cyclic structures (Zhou et al., 2018). The PEF process was developed to overcome that drawback thanks to the high photosensitivity of those complexes under UVA irradiation (Brillas, 2020). UVA photons cause the photolysis of main dissolved Fe(III) species, such as $Fe(OH)^{2+}$ via reaction (5) and metal-organic complexes from reaction (6) (El-Ghenymy et al., 2013; Alcaide et al., 2020). Note that both reactions involve the photoregeneration of Fe^{2+}, which feeds reaction (2) to enhance the $^{\bullet}OH$ production.

$$[Fe(OH)]^{2+} + h\nu \rightarrow Fe^{2+} + {}^{\bullet}OH \quad (5)$$

$$[Fe(OOCR)]^{2+} + h\nu \rightarrow Fe^{2+} + CO_2 + R^{\bullet} \quad (6)$$

On most occasions, EF and PEF treatments are carried out in undivided reactors, which is advantageous because the POPs can be additionally degraded by AO promoted by the adsorbed radicals formed on the anode surface (M) from water discharge via reaction (7) (Martinez-Huitle et al., 2015). Boron-doped diamond (BDD) (Cornejo et al., 2020) and

dimensionally stable anodes (DSA) (Lanzalaco et al., 2018) are typically employed for this purpose.

$$M + H_2O \rightarrow M(^{\bullet}OH) + H^+ + e^- \quad (7)$$

This work discusses the performance of an electrochemical reactor equipped with in-house-made 3D-like GDE as the cathode and Ir-Sn-Sb oxide as the anode, referred to the color removal and mineralization of MO solutions by PEF process as compared to AO and EF. The 3D-like GDE was used to guarantee the efficient formation of H_2O_2 and to improve the mass transport (Pérez et al., 2018). The filter-press Eco-Cell was combined in series with a UVA photoreactor, and 2 L of solution were treated under recirculation mode in each trial. The characterization of the reaction environment along the oxidation of MO in the presence of 50 mM Na_2SO_4 and 0.50 mM Fe^{2+} at pH 3.0 was systematically addressed in terms of the operation variables such as current density (*j*), volumetric flow rate (*Q*) and initial dye concentration. Carboxylic acids generated were monitored chromatographically during the PEF treatment.

2. Experimental

2.1. Chemicals

Analytical grade chemicals have been employed. Methyl Orange ($C_{14}H_{14}N_3NaO_3S$, dye content 85%, Sigma-Aldrich) played a role as model contaminant, whereas sodium sulfate (Karal) was added to ensure a high conductivity. Ferrous sulfate heptahydrate added as catalyst in EF and PEF was supplied by Fermont. All synthetic solutions were prepared with three-distilled water at room temperature (298 ± 2 K). The pH of the solutions was adjusted with diluted NaOH and H_2SO_4 solutions, both reagents acquired

from Fermont. Carboxylic acids used as standards were from Sigma-Aldrich. The solvents used for high-performance liquid chromatography (HPLC) analysis were of chromatographic grade from Karal.

2.2. Description of the flow plant

An Eco-Cell was employed as the electrochemical reactor (Fig. 1). It was equipped with a Ti|Ir-Sn-Sb oxide anode, manufactured following the Pechini method according to our recently reported procedure (Aguilar et al., 2017, 2018). Its dimensions of breadth (3.0 cm) and length (8.0 cm) conferred a total area of 24 cm^2 that contacted with the liquid phase. A 3D-like air-diffusion cathode was prepared by placing a commercial carbon cloth (ROOE Group) of 24 cm^2, previously hydrophobized with polytetrafluorethylene (PTFE) (Coria et al., 2018; Pérez et al., 2018), below a graphite felt (ROOE Group) piece (3.0 cm breadth × 8.0 cm length × 0.25 cm thickness, 651 cm^2 cm^{-3} volumetric area, 10-100 × 10^{-3} Ω^{-1} cm^{-1} electrical conductivity). The assembly was made by direct contact, without using any adhesive. A stainless-steel frame with a window of 3.0 cm breadth × 8.0 cm length × 0.23 cm thickness was used as current collector for the cathode. The back side of the carbon cloth was in contact with an air chamber (3.0 cm breadth × 8.0 cm length × 0.55 cm thickness) fed with atmospheric air pumped with a DeWalt compressor model D55168, regulating the pressure at 3 psi to electrogenerate H_2O_2. The front side of the carbon cloth and the graphite felt piece were in contact with the solution. A polypropylene separator was used in the anode side to act as flow distributor, whereas a plastic mesh (promoter type D) (Rivera et al., 2015) was placed between the anode and cathode as well as into the air chamber. An acrylic tank with capacity of 2 L was connected in series with the Eco-Cell. This reservoir was covered with a black box that contained a 15 W UVA lamp with λ_{max} = 365 nm, being turned on in PEF trials and off

in AO and EF. In AO process, the setup was the same but the GDE was replaced by a Ti|RuO_2 plate as the cathode to avoid the H_2O_2 electrogeneration. The electrochemical reactor and the reservoir were connected by hydraulic PVC pipes of 1.27 cm in diameter. The solution was recirculated by a magnetic pump (Little Giant, model 4-MD-HC) and the flow rate was adjusted by means of a PVC valve and measured with a Cole Palmer flow meter in the range of 0.5-4.0 L min^{-1}. A BK precision power supply model 1621A was used to work under galvanostatic conditions. The cell voltage was monitored with the same equipment. Fig. SM-1 depicts a sketch of the flow plant.

2.3. Methodology

To evaluate the performance of the three advanced processes, 2 L of acidic (pH 3.0) solutions containing a given concentration of MO with 50 mM Na_2SO_4, in the absence or presence of 0.50 mM Fe^{2+}, were electrolyzed in duplicate at constant *j*, *Q* and temperature. Further, the operation parameters evaluated to characterize the PEF process were *j* (10-25 mA cm^{-2}), *Q* (0.5-2.0 L min^{-1}) and the initial dye concentration (20-50 mg L^{-1} total organic carbon (TOC)). The values of catalyst concentration and pH were fixed because these have been conveniently optimized in previous works for the EF and PEF treatments of various POPs (El-Ghenymy et al., 2013; Alcaide et al., 2020).

2.4. Analytical methods

The solution pH was measured with a HANNA HI991300 pH-meter and adjusted to 3.0 with an H_2SO_4 solution (10 vol.%). The decolorization of MO solutions was monitored from the decrease of absorbance measured at the maximum (λ_{max} = 464 nm) employing a Perkin Elmer Lambda 35 UV/Vis spectrophotometer, at 298 K. The decolorization

177 percentage was determined from the starting absorbance (A_0) and its value at time *t* (A_t),
178 as follows:

179 $$\%\ \text{Color removal} = \frac{A_t - A_0}{A_0} x100 \quad (8)$$

180 Before the analysis of samples treated by EF and PEF, the pH was adjusted to ~8.0 with
181 an NaOH solution (0.25 M) to stop the Fenton's reaction thanks to the precipitation of the
182 dissolved iron. TOC was determined using a Torch combustion analyzer, from Teledyne
183 Tekmar. All samples were previously filtered using 0.45 μm cellulose nitrate syringe
184 filters supplied from Whatman. The results discussed throughout the article are the
185 average of duplicate trials and thus, the data shown in figures are accompanied by their
186 corresponding error bars.

187 The time profiles of linear carboxylic acids were assessed via ion-exclusion HPLC
188 technique, employing a Perkin Elmer Flexar liquid chromatograph (Murrieta et al., 2020).
189 The chromatograms exhibited very good peaks related to oxalic, maleic, oxamic, formic
190 and fumaric acids at retention times of 7.5, 9.4, 10.5, 14.7 and 19.3 min, respectively. The
191 electrolytic energy consumption (EC) and mineralization current efficiency (MCE) were
192 also determined (see below).

193 **3. Results and discussion**

194 *3.1. Comparative ability of AO, EF and PEF processes to degrade MO*

195 A first series of AO, EF and PEF trials was carried out to assess their oxidation power
196 during the degradation of the MO azo dye. The study of the AO degradation of solutions
197 containing MO at a TOC concentration of 30 mg L^{-1} and 50 mM Na_2SO_4 as supporting

198 electrolyte at pH 3.0 was carried out in the Eco-Cell equipped with the Ti|Ir-Sn-Sb oxide
199 anode and a Ti|RuO_2 cathode. The study of the EF and PEF processes was carried out
200 upon replacement of the Ti|RuO_2 by the 3D-like air-diffusion cathode, supplied with O_2
201 that is reduced at the cathode to form H_2O_2 via reaction (1). The same electrolyte was
202 used, but in the presence of 0.50 mM Fe^{2+}.

203 Fig. 2a shows the results obtained for the decolorization analysis at j = 20 mA cm^{-2} and
204 Q = 2.0 L min^{-1}. The color removal followed the order: AO < EF < PEF, and agreed with
205 a pseudo-first-order reaction kinetics (see inset of Fig. 2a) that yielded increasing values
206 of apparent rate constants (k_1). The constant was 0.35×10^{-2} min^{-1} (with R^2 = 0.98), 13.45
207 $\times 10^{-2}$ min^{-1} (R^2 = 0.92) and 18.04×10^{-2} min^{-1} (R^2 = 0.99) for AO, EF, PEF processes,
208 respectively. A slow color loss of the MO solution can be observed in AO, meaning that
209 the radical M($^{\bullet}$OH) formed from reaction (7) did not completely destroy the chromophore
210 group (-N=N-). Worth mentioning, during the water discharge, the oxygen evolution
211 reaction via the overall reaction (9) took place to a large extent and generated M($^{\bullet}$OH)
212 was partially converted into a weak metal oxide (Martinez-Huitle et al., 2015). This
213 behavior drastically reduced the ability of the anode to produce large quantities of reactive
214 M($^{\bullet}$OH) and, as a result, only about 80% of color removal was reached at the end of the
215 AO process. Meanwhile, in EF and PEF, the homogeneous $^{\bullet}$OH radicals produced by
216 Fenton's reaction (2) and/or photolytic reaction (5) broke rapidly the azo bond of the
217 chromophore group, yielding more than 99% decolorization after 30 min of electrolysis.

218 $$2H_2O \rightarrow 4H^+ + O_2 + 4e^- \quad (9)$$

219 Fig. 2b depicts the decrease of TOC related to MO mineralization. The AO process only
220 destroyed a 19% of TOC, whereas the EF process improved the mineralization up to a

66%. Complete MO mineralization was not achieved in the latter treatment, owing to the production of hardly oxidizable Fe(III) complexes with organic by-products. Meanwhile, in the PEF process, the mineralization was significantly upgraded thanks to the effect of UVA radiation, which accelerated the regeneration of Fe^{2+} ion from reaction (5) and quickly photodecomposed the Fe(III)-carboxylate complexes from reaction (6). Thus, TOC was reduced to 1.8 mg L^{-1}, yielding an almost total mineralization of 94%.

From the above TOC measurements, two important parameters like the mineralization current efficiency (MCE) and the energy consumption (EC) were estimated to characterize the processes. The MCE was determined according to Eq. (10), and the included parameters have been defined elsewhere (Isarain-Chávez et al., 2017; Coria et al., 2018).

$$\%\mathrm{MCE} = \frac{nFV_s\Delta(\mathrm{TOC})_{\exp}}{4.32x10^7 mlt} \times 100 \quad (10)$$

In particular, the number of carbon atoms of the initial MO was m = 14, whereas the constant number of electrons (n = 86) involved in the dye mineralization came from Eq. (11), assuming overall conversion of heteroatoms into NO_3^- and SO_4^{2-} ions:

$$C_{14}H_{14}N_3NaO_3S + 38H_2O \rightarrow 14CO_2 + 3\,NO_3^- + SO_4^{2-} + Na^+ + 90\,H^+ + 86e^- \quad (11)$$

The EC values were calculated from Eq. (12), with E_{cell} accounting for the average cell voltage (in V) (Martinez-Huitle et al., 2015; Coria et al., 2018):

$$\mathrm{EC}\ (\mathrm{kWh}\ (\mathrm{g\ TOC})^{-1}) = \frac{E_{\mathrm{cell}}It}{V_s\Delta(TOC)_{\exp}} \quad (12)$$

Fig. 2c presents the percentage of current efficiency for the assays of Fig. 2b. The highest MCE values were verified for the PEF process, with a maximal of 54% at 150 min,

242 whereupon it decayed to 23% at 420 min. This decrease of MCE is indicative of the
243 formation of more recalcitrant by-products with the simultaneous loss of organic load
244 (Brillas and Martinez-Huitle, 2015; Martínez-Huitle et al., 2015; Isarain-Chávez et al.,
245 2017). The superiority of PEF over EF is primordially due to the additional photolysis of
246 Fe(III) complexes, since in both methods, the main oxidizing agent is •OH formed from
247 Fenton's reaction (2). In contrast, much smaller MCE values varying between 5-15%
248 were determined in AO, as expected from the low oxidizing ability of M(•OH). The above
249 behavior is also reflected in the corresponding EC values given in Fig. 2d. In all cases,
250 EC increased over electrolysis time and the lowest values were obtained in the most
251 efficient process, i.e., PEF, finally obtaining 0.18 kWh (g TOC)$^{-1}$.

252 From the above results, one can establish that the PEF process was the most powerful for
253 the decolorization and mineralization of MO. The influence of current density, volumetric
254 flow rate and initial MO concentration on its performance was then systematically
255 analyzed with the purpose of finding the best operation conditions for PEF.

256 *3.2. Influence of operating parameters on PEF performance*

257 The percentage of color removal profiles with respect to electrolysis time at j values
258 between 10 and 25 mA cm^{-2}, at Q = 2.0 L min^{-1} and MO at TOC content of 30 mg L^{-1},
259 are depicted in Fig. 3a. A similar decolorization rate can be observed and more than 98%
260 color decay was always achieved at about 30 min of electrolysis. The color removal
261 followed a pseudo-first order reaction kinetics (see inset of Fig. 3a), highlighting that k_1
262 increased slightly with current density in the interval 10-20 mA cm^{-2} and then, at 25 mA
263 cm^{-2}, k_1 decreased (Table 1). From this, it can be deduced that the amount of M(•OH) and
264 •OH produced at the lowest j (10 mA cm^{-2}) was already sufficient to attack the target

pollutant and all its colored by-products. In contrast, Fig. 3b shows that TOC was more rapidly abated at 20 mA cm^{-2}, reaching a maximum mineralization of 94% at 240-300 min. A similar TOC abatement was achieved at 15 mA cm^{-2}, although much more slowly since about 420 min of electrolysis were required. The enhancement observed when *j* was increased from 10 to 20 mA cm^{-2} can be pre-eminently attributed to the higher production of H_2O_2 that caused a larger formation of $^{\bullet}OH$ from Fenton's reaction (2) and photolytic reaction (5). The quantity of Fe(III) complexes, originated more quickly, was then photolyzed earlier via reaction (6), enhancing the mineralization. However, this trend was not accomplished at 25 mA cm^{-2}, causing a quick deceleration of TOC removal. This can be associated to a faster increase in rate of the parasitic reactions involving M($^{\bullet}OH$) and $^{\bullet}OH$, diminishing their attack over organics. Examples of these unwanted reactions are the anodic oxidation of the former radical to O_2 from reaction (13), or the dimerization of the second one to H_2O_2 via reaction (14). Free $^{\bullet}OH$ can also react with the latter oxidant to form the weaker hydroperoxyl radical ($HO_2^{\bullet}$) from reaction (15), or oxidize Fe^{2+} to Fe^{3+} via reaction (16) (Brillas and Martínez-Huitle, 2015; Ye et al., 2019; Alcaide et al., 2020).

$$2M(^{\bullet}OH) \rightarrow 2M + O_2 + 2H^+ + 2e^- \quad (13)$$

$$2^{\bullet}OH \rightarrow H_2O_2 \quad (14)$$

$$H_2O_2 + {}^{\bullet}OH \rightarrow HO_2^{\bullet} + H_2O \quad (15)$$

$$Fe^{2+} + {}^{\bullet}OH \rightarrow Fe^{3+} + OH^- \quad (16)$$

Fig. 3c illustrates a larger decay of MCE as *j* became higher, which is more evident at long electrolysis time, as expected from the inverse relationship of this parameter with

current from Eq. (10). The highest MCE (95%) was found at the lowest j (10 mA cm^{-2}), dropping down to 42% at the end of the treatment. The opposite tendency can be observed in Fig. 3d for the EC values, which were gradually raised at increasing j since this was also accompanied by the concomitant increase in E_{cell}. Final values of 0.10, 0.14, 0.18 and 0.26 kWh $(g\ TOC)^{-1}$ at growing j of 10, 15, 20 and 25 mA cm^{-2}, respectively, were obtained. All these findings allow inferring that 20 mA cm^{-2} was the optimum current density for the MO treatment under the experimental conditions tested.

In a flow cell, the volumetric flow rate is a key operation parameter since the hydrodynamics regulates the mass transport of species toward the electrodes. An enhancement of the reaction rate of all electrode reactions, with generation of more quantities of H_2O_2 from reaction (1), could be expected as Q was increased, thereby yielding more $^{\bullet}OH$ (Pérez et al., 2018). This would upgrade the attack of M($^{\bullet}OH$) and $^{\bullet}OH$ over organics and the earlier photodecomposition of photoactive by-products under UVA light irradiation. To clarify this behavior, the PEF treatment of MO at TOC concentration of 30 mg L^{-1} was investigated at the optimum j = 20 mA cm^{-2} and Q values ranging between 0.5 and 2.0 L min^{-1}.

It is clear from Fig. 4a that the lowest Q (0.5 L min^{-1}) caused the poorest decolorization rate since total color removal was reached after more than 300 min of electrolysis. In contrast, Q values ≥ 1.0 L min^{-1} needed less than 60 min for total color loss. It is worth mentioning that the decolorization kinetics, was very similar at $Q \geq 1.0$ L min^{-1} (see inset of Fig. 4a), giving relatively close values of k_1 (Table 1). This points to consider that under the latter conditions, sufficient amounts of oxidizing agents were formed and rapidly transported to destroy the target pollutant, whereas at lower Q values the mass

transport of reactants toward the electrode became insufficient and the electrode reactions became slower. Fig. 4b clearly highlights the enhancement of TOC abatement at higher *Q*, in agreement with the greater generation of M(•OH) and •OH alongside the quicker photolysis of intermediates. At the end of the treatment, TOC was reduced by 60%, 75% and 80% at 0.5, 1.0 and 1.5 L min^{-1}, much lower than 94% obtained at 2.0 L min^{-1}. The same tendency can be seen for MCE in Fig. 4c, whose final values increased from 17% at 0.5 L min^{-1} to 23% at 2.0 L min^{-1}, whereas Fig. 4d evidences the progressive rise of EC up to a value of 0.28 kWh $(g\ TOC)^{-1}$ at the lowest *Q*. Hence, 2.0 L min^{-1} can be considered an optimum *Q* in PEF process.

The ability of PEF process to destroy the organic pollutants formed in MO solutions was examined at initial concentrations within the TOC range of 20-50 mg L^{-1} using the optimal j = 20 mA cm^{-2} and Q = 2.0 L min^{-1}. At all these contents, total decolorization was quickly achieved in 30-60 min of electrolysis (see Fig. 5a). Overall, the decolorization kinetics became slower as the initial TOC concentration was increased from 20 to 50 mg L^{-1} (see inset of Fig. 5a and k_1 values in Table 1). However, Fig. 5b shows that the mineralization was accelerated when initial TOC was increased from 20 to 30 mg L^{-1}, whereupon it was gradually decelerated, although a similar 79% of mineralization was attained at TOC of 20, 40 and 50 mg L^{-1}. This allows inferring a continuous rise in the quantity of TOC removed, which can be accounted for by a progressive increase of the amounts of M(•OH) and •OH that effectively reacted with MO and its by-products. Since the same quantity of these oxidizing agents is always expected in the electrolytic system because the same *j* was applied, this phenomenon can be related to the gradual decrease in reaction rate of their parasitic reactions, like reactions (13)-(16), as result of their favored attack over the larger number of organic molecules. This

behavior presupposes a concomitant growing of MCE with decreasing of EC, as can be confirmed in Fig. 5c and d, respectively. At the greatest MO concentration (TOC of 50 mg L^{-1}), these parameters reached values of 32% and 0.14 kWh (g TOC)$^{-1}$, respectively. Despite this, the most favorable mineralization occurred at TOC of 30 mg L^{-1}, when the maximum overall destruction of by-products was reached thanks to the combined action of M(•OH), •OH and UVA radiation.

3.3. Time course of final carboxylic acids

The final carboxylic acids were detected and quantified by ion-exclusion HPLC analysis of the MO solution at TOC of 30 mg L^{-1} treated by PEF under the best operation conditions, i.e., j = 20 mA cm^{-2} and Q = 2.0 L min^{-1}. Maleic, fumaric, formic, oxalic and oxamic acids were identified. Maleic and fumaric acids were generated from the cleavage of the aromatic moiety, being subsequently oxidized to formic and oxalic acids that were converted into CO_2 (Martinez-Huitle et al., 2015; Isarain-Chávez et al., 2017; Brillas, 2020). In contrast, the other final acid (oxamic) was expected from the progressive destruction of *N*-intermediates. Under the PEF conditions tested, all these acids were largely present in solution as Fe(III)-carboxylate complexes.

Fig. 6 highlights that maleic, fumaric, formic and oxamic acids were accumulated up to 0.6 mg L^{-1} as maximal, disappearing after 180 min of electrolysis. Oxalic acid was much largely accumulated, reaching 15.9 mg L^{-1} at 90 min. Then, it was rapidly removed and only a residual amount of 0.5 mg L^{-1} was detected because of the effective photolysis of Fe(III)-oxalate complexes via reaction (6). This means that the final solution with TOC of 1.8 mg L^{-1} contained TOC < 0.2 mg L^{-1} related to this acid, suggesting the formation of a small proportion (about 5.3% of initial TOC) of more recalcitrant final by-products.

Conclusions

The EF treatment of MO solutions in a flow plant led was more effective than AO, as result of the larger production of •OH in the bulk. This was feasible by the great ability of the 3D-like air-diffusion cathode to electrogenerate H_2O_2. The low oxidation power of M(•OH) generated at the Ti|Ir-Sn-Sb oxide anode explained the lower oxidation ability of AO. The PEF process was superior thanks to the continuous regeneration of Fe^{2+} catalyst induced by UVA photons. The progressive transformation of the target pollutant allowed reaching total color removal and 94% TOC abatement under optimum conditions (j = 20 mA cm^{-2} and Q = 2.0 L min^{-1}). This resulted in an MCE and EC of 35% and 0.12 kWh $(g\ TOC)^{-1}$, respectively. Small contents of maleic, fumaric, formic and oxamic acids were formed, being oxalic acid the prevailing short-chain carboxylic acid. However, it was very rapidly reduced to trace amounts (TOC < 0.2 mg L^{-1}) due to the effective photolysis of Fe(III)-oxalate species. These results confirm that the oxidation power of the PEF process with a 3D-like GDE is enough to treat azo dyes in water.

Acknowledgements

The authors gratefully acknowledge financial support from project No. CIIC 113/2020 (University of Guanajuato, Mexico) and CTQ2016-78616R (AEI/FEDER, EU). A.A. Márquez thanks CONACYT for the scholarship No. 894987 granted.

References

Aguilar, Z.G., Brillas, E., Salazar, M., Nava, J.L., Sirés, I., 2017. Evidence of Fenton-like reaction with active chlorine during the electrocatalytic oxidation of Acid Yellow 36

azo dye with Ir-Sn-Sb oxide anode in the presence of iron ion. Appl. Catal. B: Environ. 206, 44–52. https://doi.org/10.1016/j.apcatb.2017.01.006

Aguilar, Z.G., Coreño, O., Salazar, M., Sirés, I., Brillas, E., Nava, J.L., 2018. Ti|Ir–Sn–Sb oxide anode: Service life and role of the acid sites content during water oxidation to hydroxyl radicals. J. Electroanal. Chem. 820, 82–88. https://doi.org/10.1016/j.jelechem.2018.04.053

Alcaide, F., Álvarez, G., Guelfi, D.R.V., Brillas, E., Sirés, I., 2020. A stable CoSP/MWCNTs air-diffusion cathode for the photoelectro-Fenton degradation of organic pollutants at pre-pilot scale. Chem. Eng. J. 379, 122417. https://doi.org/10.1016/j.cej.2019.122417

Arshadi, M., Salimi Vahid, F., Salvacion, J.W.L., Soleymanzadeh, M., 2014. Adsorption studies of methyl orange on an immobilized Mn-nanoparticle: kinetic and thermodynamic. RSC Adv. 4, 16005–16017. https://doi.org/10.1039/C3RA47756H

Barazesh, J.M., Hennebel, T., Jasper, J.T., Sedlak, D.L., 2015. Modular advanced oxidation process enabled by cathodic hydrogen peroxide production. Environ. Sci. Technol. 49, 7391–7399. https://doi.org/10.1021/acs.est.5b01254.

Bhatia, D., Sharma, N.R., Kanwar, R., Singh, J., 2018. Physicochemical assessment of industrial textile effluents of Punjab (India). Appl. Water Sci. 8, 83. https://doi.org/10.1007/s13201-018-0728-4

Brillas, E., 2020. A review on the photoelectro-Fenton process as efficient electrochemical advanced oxidation for wastewater remediation. Treatment with UV light, sunlight, and coupling with conventional and other photo-assisted advanced technologies. Chemosphere 250, 126198. https://doi.org/10.1016/j.chemosphere.2020.126198

Brillas, E., Martínez-Huitle, C.A., 2015. Decontamination of wastewaters containing synthetic organic dyes by electrochemical methods. An updated review. Appl. Catal. B: Environ. 166, 603–643. https://doi.org/10.1016/j.apcatb.2014.11.016

Brillas, E., Sirés, I., 2015. Electrochemical removal of pharmaceuticals from water streams: Reactivity elucidation by mass spectrometry. TrAC Trends Anal. Chem. 70, 112–121. https://doi.org/10.1016/j.trac.2015.01.013

Chaiyont, R., Badoe, C., Ponce de León, C., Nava, J.L., Recio, F.J., Sirés, I., Herrasti, P., Walsh, F.C., 2013. Decolorization of Methyl Orange dye at IrO_2-SnO_2-Sb_2O_5 coated titanium anodes. Chem. Eng. Technol. 36, 123–129. https://doi.org/10.1002/ceat.201200231

Chung, K.T., 2016. Azo dyes and human health: a review. J. Environ. Sci. Heal. Part C 34, 233–261. https://doi.org/10.1080/10590501.2016.1236602

Coria, G., Pérez, T., Sirés, I., Brillas, E., Nava, J.L., 2018. Abatement of the antibiotic levofloxacin in a solar photoelectro-Fenton flow plant: Modeling the dissolved organic carbon concentration-time relationship. Chemosphere 198, 174–181. https://doi.org/10.1016/j.chemosphere.2018.01.112

Coria, G., Pérez, T., Sirés, I., Nava, J.L., 2015. Mass transport studies during dissolved oxygen reduction to hydrogen peroxide in a filter-press electrolyzer using graphite felt, reticulated vitreous carbon and boron-doped diamond as cathodes. J. Electroanal. Chem. 757, 225–229. https://doi.org/10.1016/j.jelechem.2015.09.031

Cornejo, O.M., Murrieta, M.F., Castañeda, L.F., Nava, J.L., 2020. Characterization of the reaction environment in flow reactors fitted with BDD electrodes for use in electrochemical advanced oxidation processes: A critical review. Electrochim. Acta 331, 135373. https://doi.org/10.1016/j.electacta.2019.135373

426 Cosgrove, W.J., Loucks, D.P., 2015. Water management: Current and future challenges
427 and research directions. Water Resour. Res. 51, 4823–4839.
428 https://doi.org/10.1002/2014WR016869
429 Desore, A., Narula, S.A., 2018. An overview on corporate response towards sustainability
430 issues in textile industry. Environ. Dev. Sustain. 20, 1439–1459.
431 https://doi.org/10.1007/s10668-017-9949-1
432 El-Ghenymy, A., Oturan, N., Oturan, M.A., Garrido, J.A., Cabot, P.L., Centellas, F.,
433 Rodríguez, R.M., Brillas, E., 2013. Comparative electro-Fenton and UVA
434 photoelectro-Fenton degradation of the antibiotic sulfanilamide using a stirred
435 BDD/air-diffusion tank reactor. Chem. Eng. J. 234, 115–123.
436 https://doi.org/10.1016/j.cej.2013.08.080
437 Gendel, Y., Roth, H., Rommerskirchen, A., David, O., Wessling, M., 2014. A
438 microtubular all CNT gas diffusion electrode. Electrochem. Commun. 46, 44–47.
439 https://doi.org/10.1016/j.elecom.2014.06.006
440 González-Pérez, O., Bisang, J.M., 2014. Electrochemical synthesis of hydrogen peroxide
441 with a three- dimensional rotating cylinder electrode. J. Chem. Technol. Biotechnol.
442 89, 528–535. https://doi.org/10.1002/jctb.4149
443 Guo, C., Xu, J., He, Y., Zhang, Y., Wang, Y., 2011. Photodegradation of rhodamine B
444 and methyl orange over one-dimensional TiO_2 catalysts under simulated solar
445 irradiation. Appl. Surf. Sci. 257, 3798–3803.
446 https://doi.org/10.1016/j.apsusc.2010.11.152
447 Isarain-Chávez, E., Baró, M.D., Rossinyol, E., Morales-Ortiz, U., Sort, J., Brillas, E.,
448 Pellicer, E., 2017. Comparative electrochemical oxidation of methyl orange azo dye
449 using Ti/Ir-Pb, Ti/Ir-Sn, Ti/Ru-Pb, Ti/Pt-Pd and Ti/RuO_2 anodes. Electrochim. Acta

244, 199–208. https://doi.org/10.1016/j.electacta.2017.05.101

Jiang, H., Sun, Y., Feng, J., Wang, J., 2016. Heterogeneous electro-Fenton oxidation of azo dye methyl orange catalyzed by magnetic Fe_3O_4 nanoparticles. Water Sci. Technol. 74, 1116-1126. https://doi.org/10.2166/wst.2016.300

Khan, S., Malik, A., 2018. Toxicity evaluation of textile effluents and role of native soil bacterium in biodegradation of a textile dye. Environ. Sci. Pollut. Res. 25, 4446–4458. https://doi.org/10.1007/s11356-017-0783-7

Lanzalaco, S., Sirés, I., Galia, A., Sabatino, M.A., Dispenza, C., Scialdone, O., 2018. Facile crosslinking of poly(vinylpyrrolidone) by electro-oxidation with IrO_2-based anode under potentiostatic conditions. J. Appl. Electrochem. 48, 1343–1352. https://doi.org/10.1007/s10800-018-1237-8

Lanzalaco, S., Sirés, I., Sabatino, M.A., Dispenza, C., Scialdone, O., Galia, A., 2017. Synthesis of polymer nanogels by electro-Fenton process: investigation of the effect of main operation parameters. Electrochim. Acta 246, 812–822. https://doi.org/10.1016/j.electacta.2017.06.097

Le, T.X.H., Bechelany, M., Lacour, S., Oturan, N., Oturan, M.A., Cretin, M., 2015. High removal efficiency of dye pollutants by electron-Fenton process using a graphene based cathode. Carbon 94, 1003–1011. https://doi.org/10.1016/j.carbon.2015.07.086

Lima, V.B., Goulart, L.A., Rocha, R.S., Steter, J.R., Lanza, M.R.V., 2020. Degradation of antibiotic ciprofloxacin by different AOP systems using electrochemically generated hydrogen peroxide. Chemosphere 247, 125807. https://doi.org/10.1016/j.chemosphere.2019.125807

Lin, H., Oturan, N., Wu, J., Sharma, V.K., Zhang, H., Oturan, M.A., 2017. Removal of

474 artificial sweetener aspartame from aqueous media by electrochemical advanced
475 oxidation processes. Chemosphere 167, 220–227.
476 https://doi.org/10.1016/j.chemosphere.2016.09.143
477 Martínez-Huitle, C.A., Rodrigo, M.A., Sirés, I., Scialdone, O., 2015. Single and coupled
478 electrochemical processes and reactors for the abatement of organic water pollutants:
479 a critical review. Chem. Rev. 115, 13362–13407.
480 https://doi.org/10.1021/acs.chemrev.5b00361
481 McDonald, R.I., Weber, K., Padowski, J., Flörke, M., Schneider, C., Green, P.A.,
482 Gleeson, T., Eckman, S., Lehner, B., Balk, D., Boucher, T., Grill, G., Montgomery,
483 M., 2014. Water on an urban planet: Urbanization and the reach of urban water
484 infrastructure. Glob. Environ. Chang. 27, 96–105.
485 https://doi.org/10.1016/j.gloenvcha.2014.04.022
486 Murrieta, M.F., Sirés, I., Brillas, E., Nava, J.L., 2020. Mineralization of Acid Red 1 azo
487 dye by solar photoelectro-Fenton-like process using electrogenerated HClO and
488 photoregenerated Fe(II). Chemosphere 246, 125697.
489 https://doi.org/10.1016/j.chemosphere.2019.125697
490 Omri, A., Hamza, W., Benzina, M., 2020. Photo-Fenton oxidation and mineralization of
491 methyl orange using Fe-sand as effective heterogeneous catalyst. J. Photochem.
492 Photobiol. A: Chem. 393, 112444.
493 https://doi.org/10.1016/j.jphotochem.2020.112444
494 Pérez, T., Coria, G., Sirés, I., Nava, J.L., Uribe, A.R., 2018. Electrosynthesis of hydrogen
495 peroxide in a filter-press flow cell using graphite felt as air-diffusion cathode. J.
496 Electroanal. Chem. 812, 54–58. https://doi.org/10.1016/j.jelechem.2018.01.054
497 Rawat, D., Mishra, V., Sharma, R.S., 2016. Detoxification of azo dyes in the context of

498 environmental processes. Chemosphere 155, 591–605.
499 https://doi.org/10.1016/j.chemosphere.2016.04.068
500 Rivera, F.F., de León, C.P., Walsh, F.C., Nava, J.L., 2015. The reaction environment in
501 a filter-press laboratory reactor: the FM01-LC flow cell. Electrochim. Acta 161,
502 436–452. https://doi.org/0.1016/j.electacta.2015.02.161
503 Routoula, E., Patwardhan, S. V, 2020. Degradation of anthraquinone dyes from effluents:
504 a review focusing on enzymatic dye degradation with industrial potential. Environ.
505 Sci. Technol. 54, 647–664. https://doi.org/10.1021/acs.est.9b03737
506 Salmerón, I., Plakas, K. V., Sirés, I., Oller, I., Maldonado, M.I., Karabelas, A.J., Malato,
507 S., 2019. Optimization of electrocatalytic H_2O_2 production at pilot plant scale for
508 solar-assisted water treatment. Appl. Catal. B: Environ. 242, 327–336.
509 https://doi.org/10.1016/j.apcatb.2018.09.045
510 Saravanan, R., Manoj, D., Qin, J., Naushad, M., Gracia, F., Lee, A.F., Khan, M.M.,
511 Gracia-Pinilla, M.A., 2018. Mechanothermal synthesis of Ag/TiO_2 for
512 photocatalytic Methyl Orange degradation and hydrogen production. Process Saf.
513 Environ. Prot. 120, 339–347. https://doi.org/10.1016/j.psep.2018.09.015
514 Scialdone, O., Galia, A., Gattuso, C., Sabatino, S., Schiavo, B., 2015. Effect of air
515 pressure on the electro-generation of H_2O_2 and the abatement of organic pollutants
516 in water by electro-Fenton process. Electrochim. Acta 182, 775–780.
517 https://doi.org/10.1016/j.electacta.2015.09.109
518 Sirés, I., Low, C.T.J., Ponce de León, C., Walsh, F., 2010. The deposition of
519 nanostructured β-PbO_2 coatings from aqueous methanesulfonic acid for the
520 electrochemical oxidation of organic pollutants. Electrochem. commun. 12, 70–74.
521 https://doi.org/10.1016/j.elecom.2009.10.038

Tkaczyk, A., Mitrowska, K., Posyniak, A., 2020. Synthetic organic dyes as contaminants of the aquatic environment and their implications for ecosystems: A review. Sci. Total Environ. 717, 137222. https://doi.org/10.1016/j.scitotenv.2020.137222

Yang, W., Zhou, M., Oturan, N., Li, Y., Su, P., Oturan, M.A., 2019. Enhanced activation of hydrogen peroxide using nitrogen doped graphene for effective removal of herbicide 2,4-D from water by iron-free electrochemical advanced oxidation. Electrochim. Acta 297, 582–592. https://doi.org/10.1016/j.electacta.2018.11.196

Ye, Z., Guelfi, D.R.V., Álvarez, G., Alcaide, F., Brillas, E., Sirés, I., 2019. Enhanced electrocatalytic production of H_2O_2 at Co-based air-diffusion cathodes for the photoelectro-Fenton treatment of bronopol. Appl. Catal. B: Environ. 247, 191–199. https://doi.org/10.1016/j.apcatb.2019.01.029

Yu, X., Zhou, M., Ren, G., Ma, L., 2015. A novel dual gas diffusion electrodes system for efficient hydrogen peroxide generation used in electro-Fenton. Chem. Eng. J. 263, 92–100. https://doi.org/10.1016/j.cej.2014.11.053

Zhou, M., Oturan, M.A., Sires, I., 2018. Electro-Fenton Process: New Trends and Scale Up. Springer Nature, Singapore.

Zhou, M., Särkkä, H., Sillanpää, M., 2011. A comparative experimental study on methyl orange degradation by electrochemical oxidation on BDD and MMO electrodes. Sep. Purif. Technol. 78, 290–297. https://doi.org/10.1016/j.seppur.2011.02.013

Zhou, W., Rajic, L., Zhao, Y., Gao, J., Qin, Y., Alshawabkeh, A.N., 2018. Rates of H_2O_2 electrogeneration by reduction of anodic O_2 at RVC foam cathodes in batch and flow-through cells. Electrochim. Acta 277, 185–196. https://doi.org/10.1016/j.electacta.2018.04.174

546 **Figure captions**

547 **Figure 1**. Diagram of the electrochemical reactor showing the labelled components.

548 **Figure 2.** Change of (a) color removal, (b) normalized TOC content, (c) mineralization
549 current efficiency and (d) electrolytic energy consumption with electrolysis time during
550 different treatments: (◊) AO, (○) EF and (Δ) PEF. Conditions: 2 L of a solution with MO
551 at a concentration of 30 mg L^{-1} of TOC, 50 mM Na_2SO_4 and 0.50 mM Fe^{2+} at pH 3.0,
552 treated at Q = 2.0 L min^{-1} and j = 20 mA cm^{-2}. The inset in plot (a) shows the pseudo-
553 first-order kinetic analysis for MO decolorization.

554 **Figure 3.** Change of (a) color removal (see kinetic analysis in the inset), (b) TOC, (c)
555 mineralization current efficiency and (d) electrolytic energy consumption with
556 electrolysis time for PEF treatments at different j: (◊) 10, (○) 15, (Δ) 20 and (∇) 25 mA
557 cm^{-2}. Same conditions as described in Fig. 2.

558 **Figure 4.** Effect of the volumetric flow rate under the same conditions described in Fig.
559 3, at 20 mA cm^{-2}. Q: (◊) 0.5, (○) 1.0, (Δ) 1.5 and (∇) 2.0 L min^{-1}. The inset in plot (a)
560 shows the pseudo-first-order kinetic analysis for MO decolorization.

561 **Figure 5.** Effect of the initial dye concentration under the same conditions described in
562 Fig. 3, at 20 mA cm^{-2}. [MO]: (◊) 20, (○) 30, (Δ) 40 and (∇) 50 mg L^{-1} of TOC. See the
563 kinetic analysis in the inset of plot (a).

564 **Figure 6.** Time course of the concentration of (■) oxalic, (●) maleic, (▲) oxamic, (▼)
565 formic and (♦) fumaric acids during the mineralization of the MO solution by PEF under
566 the conditions described in Fig. 2. The inset shows a magnification of the same profiles.

567

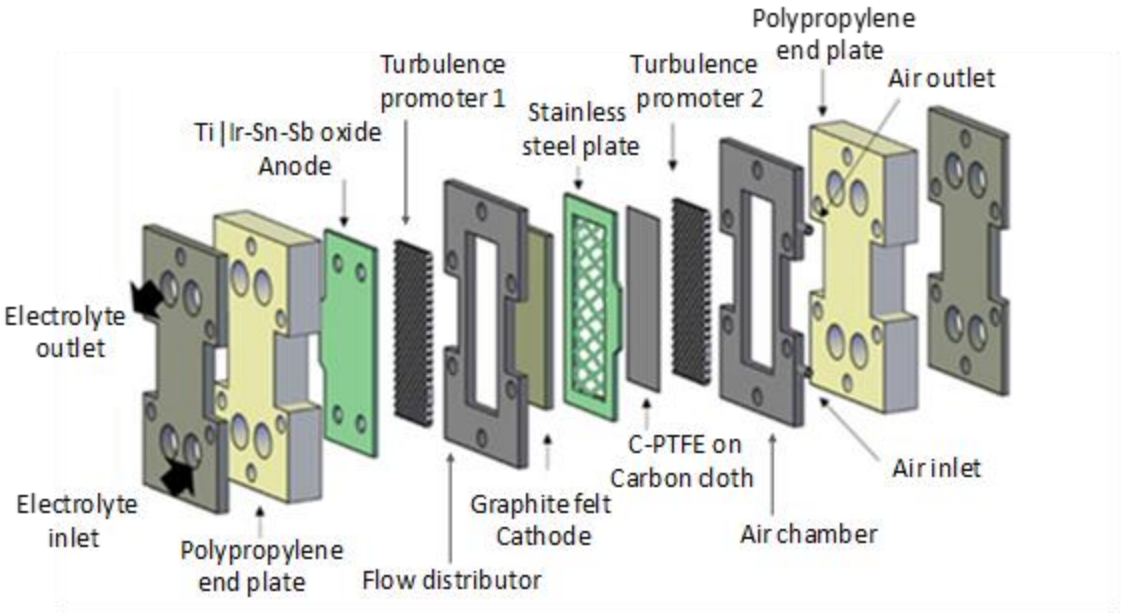
Polypropylene
end plate
Air outlet
Turbulence
promoter 1
Turbulence
promoter 2
Stainless
steel plate
Ti|Ir-Sn-Sb oxide
Anode
Electrolyte
outlet
C-PTFE on
Carbon cloth
Air inlet
Electrolyte
inlet
Graphite felt
Cathode
Air chamber
Polypropylene
end plate
Flow distributor

Figure 1

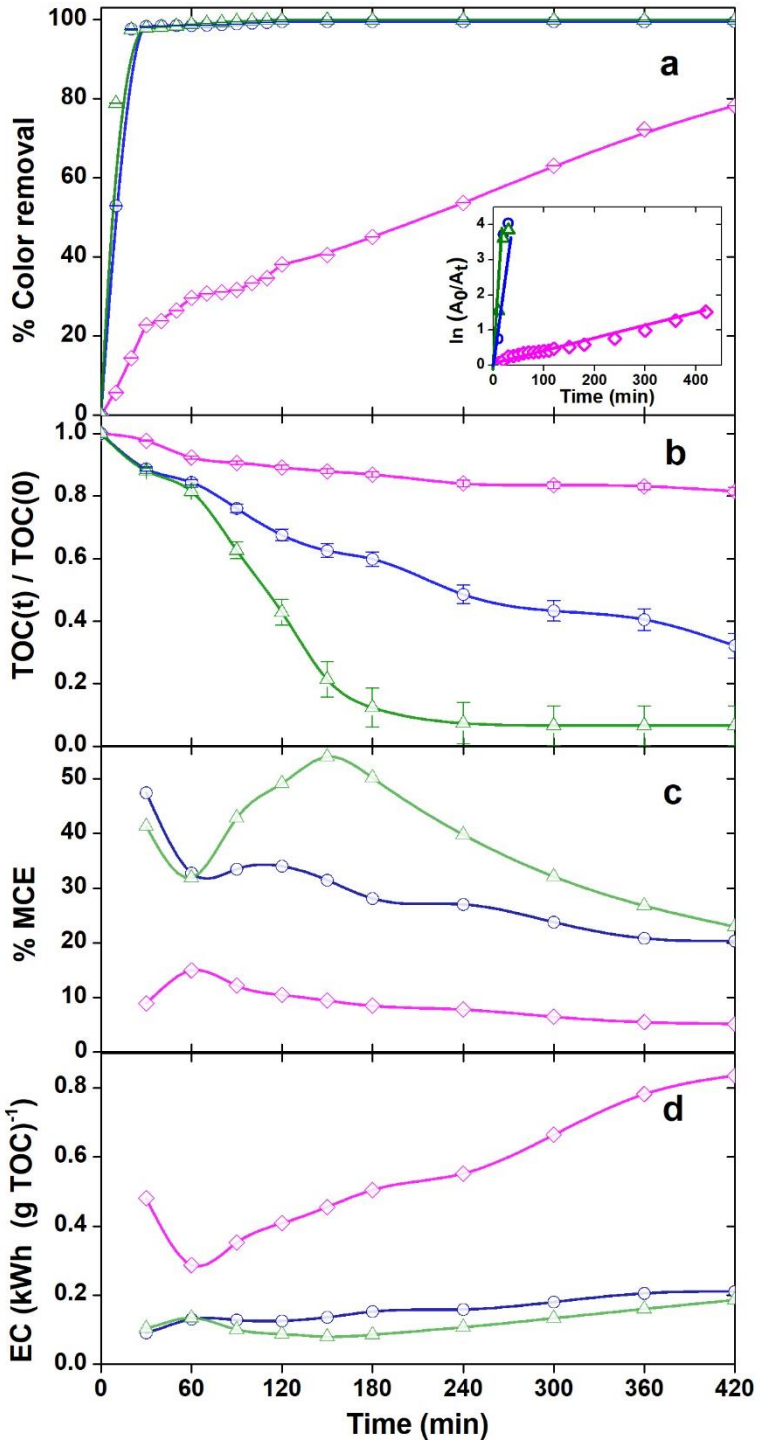
a
% Color removal
ln (A0/At)
Time (min)
b
TOC(t) / TOC(0)
c
% MCE
d
EC (kWh (g TOC)-1)
Time (min)

Figure 2

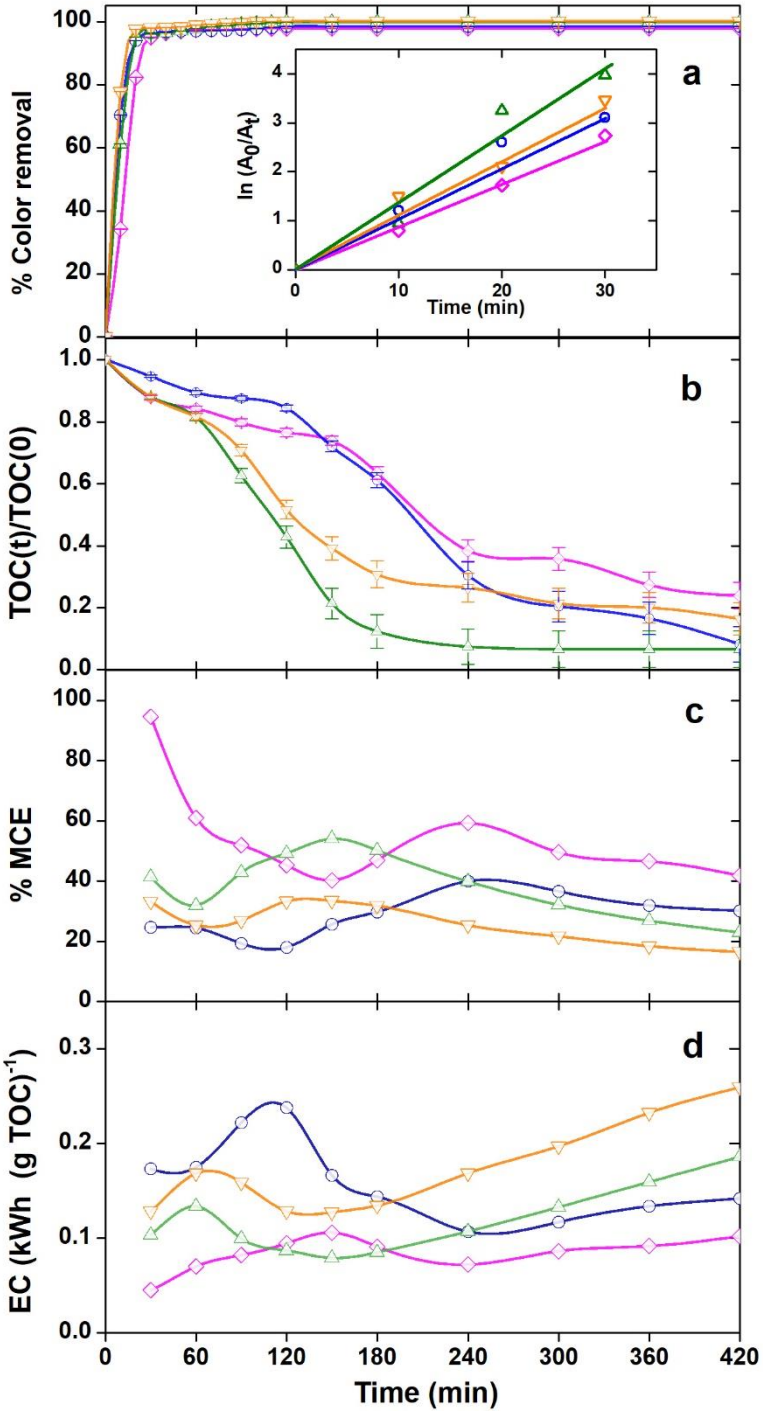
a
% Color removal
ln (A0/At)
Time (min)
b
TOC(t)/TOC(0)
c
% MCE
d
EC (kWh (g TOC)-1)
Time (min)

Figure 3

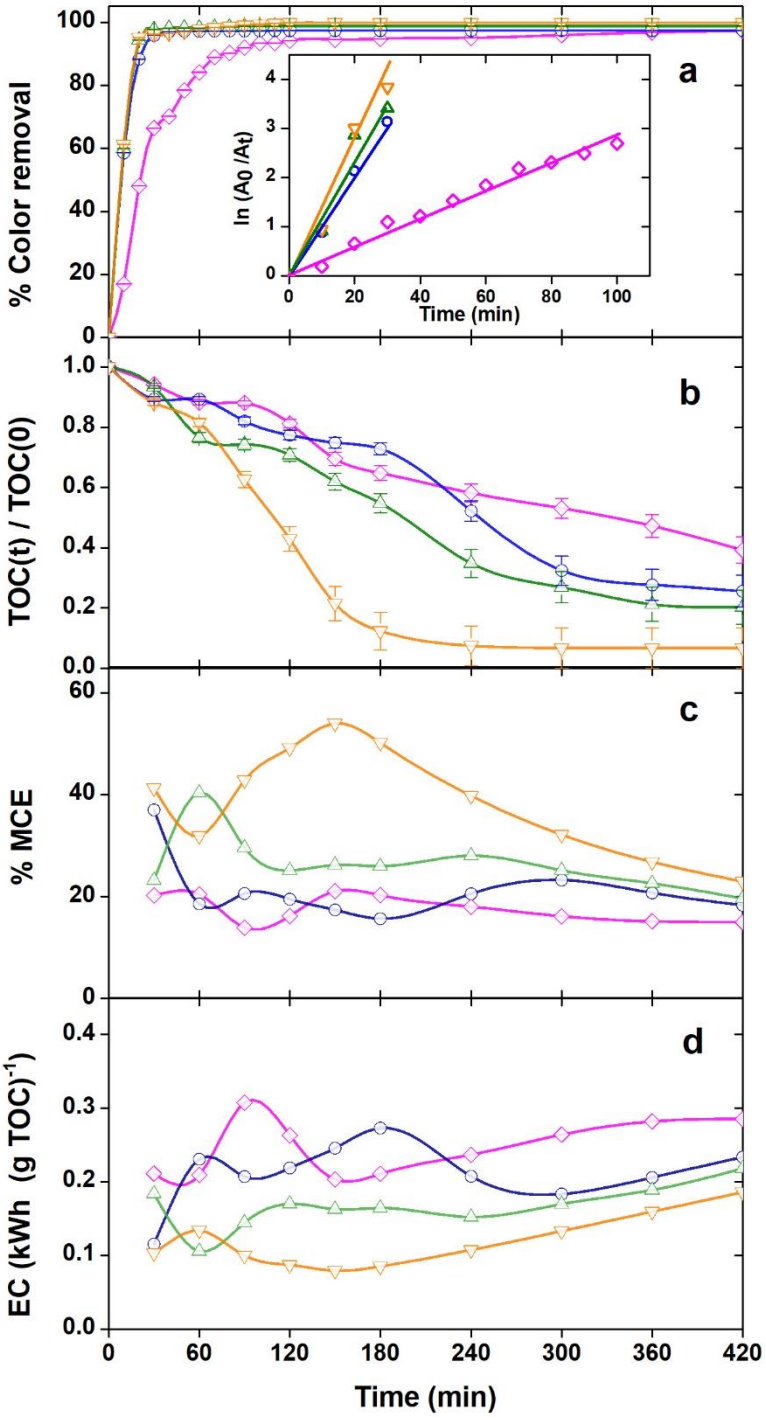
a
% Color removal
ln (A0 /At)
Time (min)
b
TOC(t) / TOC(0)
c
% MCE
d
EC (kWh (g TOC)-1)
Time (min)

Figure 4

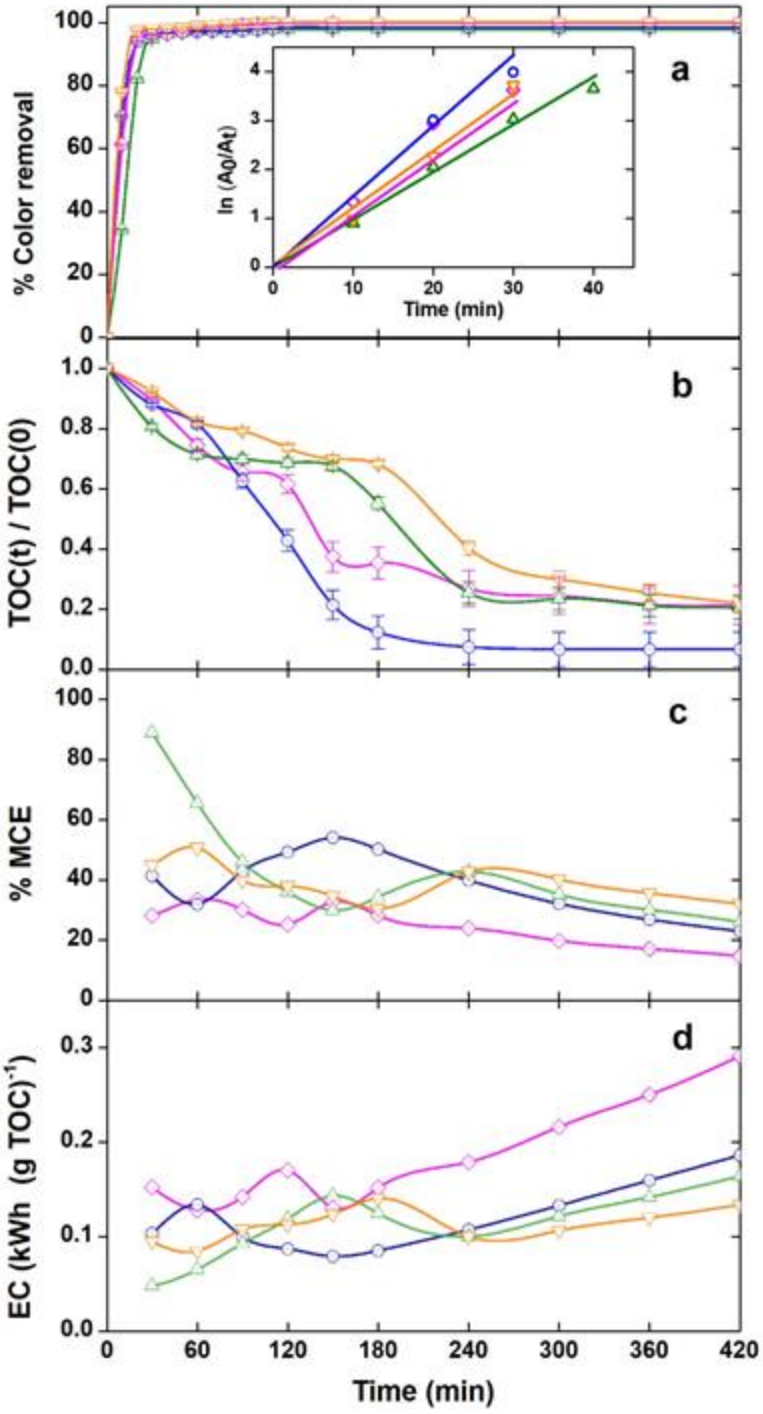
a
% Color removal
ln (A0/At)
Time (min)
b
TOC(t) / TOC(0)
c
% MCE
d
EC (kWh (g TOC)-1)
Time (min)

Figure 5

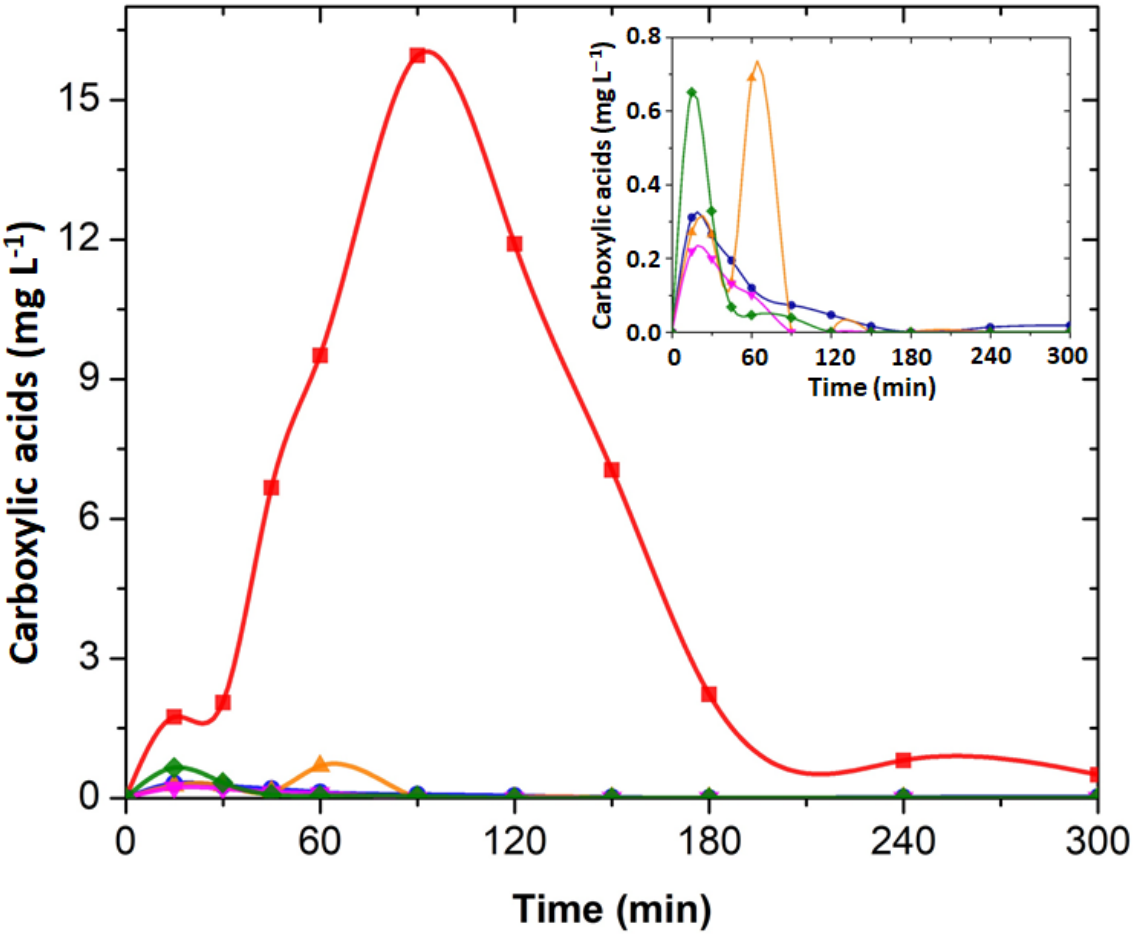
Carboxylic acids (mg L-1)
Time (min)
0
3
6
9
12
15
0
60
120
180
240
300
Carboxylic acids (mg L−1)
Time (min)
0.0
0.2
0.4
0.6
0.8

Figure 6

Table 1. Pseudo-first-order rate constants and *R*-squared values, along with the percentage of TOC removal and energy consumption per unit TOC mass for the PEF treatment of 2 L of MO solutions in the presence of 0.5 mM Fe^{2+} at pH 3.0 and 298 ± 2 K, using the ECO-cell with an Ir-Sn-Ru oxide anode and a 3D-like air-diffusion cathode.

j (mA cm^{-2})	TOC(0) (mg L^{-1})	Q (L min^{-1})	k_1 (10^{-2} min^{-1})	R^2	% TOC removal	EC (kWh $(gTOC)^{-1}$)
10	30	2.0	8.22	0.96	76.2	0.84
15	30	2.0	11.01	0.97	91.9	1.62
20	20	2.0	10.95	0.95	78.7	1.81
	30	0.5	2.70	0.98	60.9	2.47
		1.0	10.45	0.99	74.5	2.12
		1.5	12.48	0.97	79.8	1.65
		2.0	18.04	0.99	93.5	1.17
	40	2.0	9.13	0.90	79.6	1.12
	50	2.0	12.07	0.95	78.1	1.12
25	30	2.0	12.87	0.93	83.7	1.70